Fibrinogen Induces Microglia-Mediated Spine Elimination and Cognitive Impairment in an Alzheimer's Disease Model

Mario Merlini[1], **Victoria A. Rafalski**[1], **Pamela Rios E. Coronado**[1], **T. Michael Gill**[1], **Maya Ellisman**[1], **Gayathri Muthukumar**[1], **Keshav S. Subramanian**[1], **Jae Kyu Ryu**[1], **Catriona A. Syme**[1], **Dimitrios Davalos**[1,4], **William W. Seeley**[2], **Lennart Mucke**[1,2], **Robert B. Nelson**[3,5], and **Katerina Akassoglou**[1,2,6,*]

[1]Gladstone Institute of Neurological Disease, San Francisco, CA 94158, USA

[2]Department of Neurology, University of California, San Francisco, San Francisco, CA 94158, USA

[3]Lundbeck Research USA, Paramus, NJ 07652, USA

SUMMARY

Cerebrovascular alterations are a key feature of Alzheimer's disease (AD) pathogenesis. However, whether vascular damage contributes to synaptic dysfunction and how it synergizes with amyloid pathology to cause neuroinflammation and cognitive decline remain poorly understood. Here we show that the blood protein fibrinogen induces spine elimination and promotes cognitive deficits by CD11b/CD18-mediated microglia activation. 3D molecular labeling in cleared mouse and human AD brains combined with repetitive in vivo two-photon imaging showed focal fibrinogen deposits associated with loss of dendritic spines independent of amyloid plaques. Fibrinogen-induced spine elimination was prevented by inhibiting reactive oxygen species (ROS) generation or genetic ablation of CD11b. Genetic elimination of the fibrinogen binding motif to CD11b reduced neuroinflammation, synaptic deficits, and cognitive decline in the 5XFAD mouse model of AD. Thus, fibrinogen-induced spine elimination and cognitive decline via CD11b link

cerebrovascular damage with immune-mediated neurodegeneration and may have important implications in AD and related conditions.

Graphical Abstract
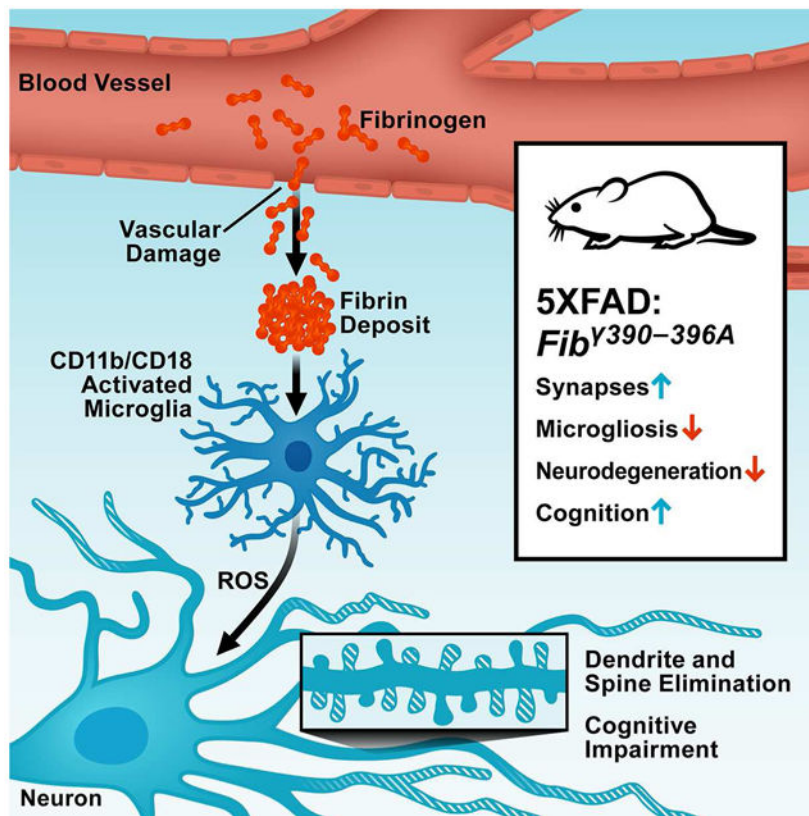
eTOC

Vascular pathology is a key feature of Alzheimer's disease. Merlini et al. identify that the blood protein fibrinogen induces microglia-mediated spine elimination and cognitive decline. These fibrinogen effects are mediated by reactive oxygen species and are independent of Aβ plaques.

INTRODUCTION

Alzheimer's disease (AD) is characterized by cerebral amyloid-β (Aβ) deposition, vascular alterations, tau pathology, microglia activation, and inflammation (De Strooper and Karran, 2016). Intriguingly, vascular dysfunction and amyloid burden are independent and equal predictors of cognitive decline in the elderly, with an additive adverse effect on cognition (Rabin et al., 2018; Vemuri et al., 2015). Cerebrovascular damage can occur in the absence of Aβ and can precede plaque formation (Merlini et al., 2016; Vemuri et al., 2015). Intracerebral microhemorrhages/microbleeds are a manifestation of vascular damage that correlate with the conversion of mild cognitive impairment (MCI) to AD and predict memory impairment (Akoudad et al., 2016). Blood-brain barrier (BBB) disruption is detected in MCI and early AD and correlates with disease progression (Montagne et al.,

2017). Compromised vascular integrity and microbleeds result in the influx of blood proteins into the CNS (Sweeney et al., 2018). However, the vascular mechanisms underlying neuronal dysfunction remain poorly understood, and the relationship between vascular dysfunction, blood-derived proteins and Aβ in the AD brain is not known.

Fibrinogen, a blood coagulation protein, is deposited in the AD brain, co-localizes with amyloid plaques, pericyte loss, dystrophic neurites, and activated microglia, and its increased concentrations in plasma and cerebrospinal fluid correlates with brain atrophy in AD patients (Petersen et al., 2018; Strickland, 2018). Consistent with human data, CNS fibrin deposition occurs in multiple animal models of AD and is a feature of the progressive neurodegeneration in pericyte-deficient and *APOE* transgenic models (Montagne et al., 2017). Fibrinogen binds the CD11b/CD18 integrin receptor (a.k.a. complement receptor 3 [CR3], Mac-1, αMβ2) and induces pathogenic microglia activation (Petersen et al., 2018). Fibrinogen also binds Aβ, and pharmacologic or genetic fibrinogen depletion reduces cognitive decline and neuropathology in AD models (Cortes-Canteli et al., 2010; Montagne et al., 2018). Despite compelling evidence that fibrinogen can interact with Aβ and exacerbate its effects, it remains unknown whether fibrinogen-induced neuroinflammation promotes cognitive decline after vascular dysfunction. Here we tested the contribution of fibrinogen-induced microglia activation to spine elimination and cognitive impairment in AD using 3D molecular labeling and volume imaging of cleared brains from mice and humans with AD, longitudinal two-photon (2P) in vivo microscopy, and behavioral testing in mouse models.

RESULTS

Dendritic Spine Elimination occurs around Fibrinogen Deposits in AD Mice

To test whether fibrinogen contributes to neuronal deficits in AD-relevant mouse models ("AD mice"), we performed repeated in vivo 2P imaging over 14 days of Aβ deposits, fibrinogen, dendrites and dendritic spines in the cortex of 5XFAD mice, which co-express five familial AD mutations and rapidly develop severe amyloid pathology (Oakley et al., 2006). Fibrinogen deposits were detected both in proximity to and distal from Aβ plaques (Figure 1A). Notably, dendritic spine elimination occurred around fibrinogen deposits even distal from Aβ plaques (Figure 1A, Fibrinogen). As reported (Tsai et al., 2004), dendritic spine loss occurred around Aβ deposits, and was similar around Aβ deposits with or without fibrinogen (Figure 1A, Aβ and Aβ with fibrinogen). Dendrites at >50 μm from an Aβ or a fibrinogen deposit did not show spine changes (Figure 1A, No deposits). Similar findings were made in an independent hAPP transgenic mouse model (hAPP-J20 mice) (Mucke et al., 2000) (Figure S1). These results show that fibrinogen is associated with dendritic spine elimination in AD mice even in areas distal from Aβ deposits.

Using immunolabeling-enabled 3D imaging of solvent-cleared organs (iDISCO) (Renier et al., 2014), we studied in large brain volumes the spatiotemporal distribution between fibrinogen, Aβ, and vasculature in mouse and human AD brains. Fibrinogen was present as cortical and hippocampal parenchymal deposits in 5XFAD and hAPP-J20 mice (Figures 1B and S2; Videos S1 and S2). Hippocampal fibrinogen deposits in 5XFAD mice increased with age (Figure 1B), and were absent in wild-type (WT) or fibrinogen-deficient (*Fga*⁻/⁻) mice,

and in anti-fibrinogen antibody omission controls (Figure 1B, Figure S2C and S2E). Staining of the choroid plexus/ventricles, meninges and blood vessels in superficial cortical layers was observed in 5XFAD, WT, and *Fga*^{−/−} mouse brains, suggestive of non-specific edge-effect and it was not included in the analysis (Figure S2D).

In post-mortem neocortex from patients with AD, combined 3D volume imaging of fibrinogen, blood vessels, and Aβ showed intravascular, vessel-associated and parenchymal fibrinogen in regions with and without Aβ deposits (Figures 1C–1E, S3D–S3F, Video S3). Vessel-associated fibrinogen was defined as vascular or perivascular deposits present at the abluminal side of CD31-stained vessels. Tortuous vascular structures with vessel-associated fibrinogen deposits were found in three of the five AD brains analyzed (Figures 1E, S3F, and Video S3). As expected, age-matched non-demented control (NDCTRL) brains had mainly intravascular fibrinogen (Figures 1F and S3A–C). Parenchymal fibrinogen deposits were detected in NDCTRL to a lesser extent than in AD brains (Figures 1F, S3A–C, and Video S3). Aβ was not detected in NDCTRL brains (Figures 1F, S3A-C). Collectively, our results show widespread fibrinogen deposition in the AD brain that colocalizes with dendritic spine loss even in areas devoid of Aβ deposits.

Fibrinogen Induces Dendrite Loss and Spine Elimination in the Healthy Brain

To test whether fibrinogen is sufficient to induce spine loss independent of Aβ pathology, we longitudinally imaged dendrites and spines in the cortex of *Thy1-YFP* mice after injection of fibrinogen with a glass microelectrode. At physiological blood concentrations, cortically injected human fibrinogen caused localized dendrite and spine loss by day 3 post-injection, compared to baseline and artificial cerebrospinal fluid (ACSF) vehicle control (Figures 2A and 2B). Similar results were obtained with mouse fibrinogen (Figures S4A and 4B), suggesting no species differences. Like fibrinogen, WT plasma also induced dendrite and spine loss (Figures 2C and 2D). In contrast, dendrite and spine loss was reduced after injection of fibrinogen-deficient (*Fga*^{−/−}) plasma, which contains all plasma proteins except fibrinogen (Figures 2C and 2D). Together, our results suggest that cerebral extravasation of blood proteins causes neurite loss and that fibrinogen is a major mediator of this effect.

Fibrinogen induces Dendrite and Spine Loss through Microglial CD11b Receptor Activation and ROS Generation

To determine whether microglia contribute to fibrinogen-induced spine elimination, we performed simultaneous longitudinal imaging of microglia and dendrites in the cortex of *Thy1-YFP:Cx3cr1*[GFP/+] mice after fibrinogen injection. Compared to baseline or vehicle controls, fibrinogen injection caused microglia activation as evidenced by amoeboid microglia with reduced processes (Figure 2E and Video S4). Fibrinogen-induced microglia activation is mediated by fibrinogen binding to CD11b (encoded by *Itgam*) (Petersen et al., 2018). Loss of CD11b prevented fibrinogen-induced dendrite and spine loss in *Thy1-YFP.Itgam*^{−/−} mice (Figures 3A and 3B), suggesting that fibrinogen-induced spine elimination is microglia-dependent. Fibrinogen-induced CD11b/CD18 receptor-mediated microglia activation instigates the generation and release of neurotoxic reactive oxygen species (ROS) via nicotinamide adenine dinucleotide phosphate (NADPH) oxidase, which is upregulated in neurodegenerative diseases (Haslund-Vinding et al., 2017; Lassmann, 2011;

Ryu et al., 2018). Longitudinal in vivo imaging revealed fibrinogen-induced ROS release and dendrite loss at sites of microglia activation (Figure 3C, Video S4). Inhibition of ROS release by the NADPH inhibitor apocynin (Haslund-Vinding et al., 2017) prevented fibrinogen-induced dendrite and spine loss (Figures 3D and 3E). These results suggest that fibrinogen induces dendrite and spine loss through an oxidative damage-causing pathway involving CD11b-dependent microglia activation.

Genetic Disruption of Fibrinogen-CD11b Receptor Binding Prevents Neurodegeneration and Cognitive Impairment

To test the effects of fibrinogen-CD11b receptor binding on cognitive impairment, we crossed 5XFAD with $Fgg^{\gamma 390-396A}$ knock-in mice, which express fully coagulable fibrinogen that selectively lacks the CD11b receptor binding site (Adams et al., 2007; Flick et al., 2004). We compared learning and memory in 10-month-old 5XFAD, 5XFAD:$Fgg^{\gamma 390-396A}$, $Fgg^{\gamma 390-396A}$, and littermate non-transgenic wild-type (WT) mice (Figures 4A, S4C, and S4D). In the active place avoidance test, which measures amygdala/ hippocampus-dependent visual-spatial learning and memory (Pastalkova et al., 2006), 5XFAD mice showed severe learning and memory impairments, whereas 5XFAD:$Fgg^{\gamma 390-396A}$ performed as well as WT and $Fgg^{\gamma 390-396A}$ control mice (Figure 4A). 5XFAD mice, but not 5XFAD:$Fgg^{\gamma 390-396A}$ mice, also displayed hyperactivity in the open field test (Figure S4C). No differences were observed in the hot plate test (Figure S4D), suggesting that the differences among genotypes in the active place avoidance test were not caused by differences in pain perception. In all behavioral paradigms, $Fgg^{\gamma 390-396A}$ mice performed similarly to WT controls (Figures 4A, S4C, and S4D).

5XFAD mice had loss of MAP2+ neurons and presynaptic terminals in the hippocampus that were reduced on the $Fgg^{\gamma 390-396A}$ background (Figure 4B). Iba-1+ microglia and the dystrophic neurite/lysosomal marker LAMP-1 were reduced in 5XFAD:$Fgg^{\gamma 390-396A}$ compared to 5XFAD mice (Figure 4B). Consistent with prior studies of genetic depletion of either fibrinogen or CD11b in AD models (Cortes-Canteli et al., 2010; Czirr et al., 2017), Aβ plaque burden was decreased in the hippocampus of 5XFAD:$Fgg^{\gamma 390-396A}$ mice (Figure 4B). Hippocampal Aβ deposition, neuronal loss, increased LAMP-1, and microglia activation in 5XFAD mice were in line with prior studies (Gowrishankar et al., 2015; Oakley et al., 2006). No significant differences were observed in the cortex of 5XFAD:$Fgg^{\gamma 390-396A}$ mice compared to 5XFAD mice at 10 months of age (not shown). Thus, genetic mutation of the fibrinogen binding motif to CD11b reduces features of neurodegeneration and cognitive decline in 5XFAD mice.

DISCUSSION

Our study provides a link between vascular pathology and cognitive decline by identifying the blood protein fibrinogen as a trigger of microglia-dependent spine elimination, dendrite loss, and cognitive impairment in an AD-relevant context. Fibrinogen induced microglia-dependent spine elimination in WT brain, indicating that fibrinogen is sufficient to impair neurons even in the absence of abnormal Aβ accumulation. As a proinflammatory clotting factor deposited in the AD brain, fibrinogen may act in parallel to Aβ in promoting spine

elimination and cognitive performance. These findings shed mechanistic light on clinical studies suggesting that vascular pathology is independent of, but additive to, Aβ load in mediating cognitive decline (Rabin et al., 2018; Vemuri et al., 2015). Since Aβ-fibrinogen binding blocks fibrin degradation (Cortes-Canteli et al., 2010), Aβ may promote fibrin-induced neurodegeneration by sustaining fibrin deposition in the CNS, thus enhancing chronic CD11b-mediated microglia activation. Conversely, fibrinogen/CD11b signaling may enhance Aβ-induced neurodegeneration by suppressing Aβ clearance (Czirr et al., 2017). Furthermore, fibrinogen binds soluble, non-fibrillar amyloid species (Zamolodchikov et al., 2016), which are concentrated around vessels affected by cerebral amyloid angiopathy (CAA) (Shinkai et al., 1995) and induce spine loss (Kirkwood et al., 2013). Since CAA appears to be a chief contributor to BBB leakage in humans and mouse models of cerebral amyloidosis (Hartz et al., 2012), CAA could promote fibrinogen extravasation and fibrinogen-dependent spine elimination. Future studies will determine the relative contributions of fibrinogen and soluble amyloid species to spine elimination in CAA.

Microglia may have pathogenic and protective roles in AD through toxic effects on neurons, participating in Aβ clearance, or limiting plaque size (Butovsky and Weiner, 2018; De Strooper and Karran, 2016). Our study suggests that fibrinogen at sites of vascular damage induces a pathogenic microglia response to promote spine loss and cognitive decline. Dendritic spines are critical for learning and memory and their number correlates with cognitive resilience in AD patients (Boros et al., 2017). Fibrinogen-induced spine elimination was prevented in *Itgam*−/− mice, suggesting that CD11b/CD18 receptor activation is required for fibrinogen-induced spine loss. Since mutation of the CD11b binding site of fibrinogen in 5XFAD: *Fggγ390–396A* mice was sufficient to inhibit cognitive deficits, fibrinogen binding to CD11b is required for neuropathological changes in AD. Besides fibrinogen, CD11b/CD18 binds several structurally unrelated ligands including complement (Haslund-Vinding et al., 2017). Thus, fibrinogen-induced ROS release and spine elimination (this study) may act in parallel with complement-induced phagocytosis of spines (Hong et al., 2016) to eliminate synapses. Since fibrinogen and complement bind to the same receptor, the stoichiometry, bioavailability, and temporal regulation of the two ligands might influence signaling downstream of CD11b/CD18. Potentially, at sites of BBB disruption, fibrinogen-induced ROS release may modulate phagocytosis-independent synapse remodeling (Weinhard et al., 2018). Future studies will determine how at sites of vascular damage CD11b/CD18 integrates signaling from multiple ligands to contribute to spine elimination via oxidative and phagocytic mechanisms.

Fibrinogen-induced microglia activation is also pathogenic in animal models of MS (Petersen et al., 2018). Although the patterns of microglia activation are distinct between AD and MS (Butovsky and Weiner, 2018), fibrinogen-induced activation of pro-oxidant pathways in innate immune cells may be a shared mechanism of neuronal dysfunction in MS and AD (Lassmann, 2011; Petersen et al., 2018; Ryu et al., 2018), as synaptic pathology and microglia-mediated oxidative stress occur in both diseases (Haslund-Vinding et al., 2017; Lassmann, 2011). Indeed, *Fggγ390–396A* mice have reduced neurodegeneration and microglia activation in an MS model (Adams et al., 2007; Davalos et al., 2012) and in an AD model (this study). Fibrinogen injection in myelinated areas promotes myelin loss (Ryu et al., 2015), while cortical fibrinogen injection induces microglia-mediated dendrite loss and

spine elimination (this study). Thus, fibrinogen-mediated brain pathology may be region-specific and relate to the degree of BBB permeability. The contribution of fibrin to white matter alterations, such as those in pericyte-deficient mice or MS models (Montagne et al., 2018; Petersen et al., 2017; Ryu et al., 2015), may have bearing on AD given the prominence of white matter hyperintensities therein (Barker et al., 2014). Future studies will compare the consequences of fibrin-induced microglia activation in white and gray matter at a systems level in MS and AD models.

Our study identifies 3D volume imaging of fibrinogen as a sensitive detector of vascular abnormalities in AD. The highly focal fibrinogen deposition pattern we observed in cleared mouse and human brain supports the emerging recognition that cerebrovascular damage, microbleeds and BBB disruption are key features of AD (Sweeney et al., 2018). Fibrinogen is unique among other blood proteins as it clots and forms an insoluble proinflammatory fibrin deposit in the CNS (Petersen et al., 2018). The focal pattern of BBB leakage and fibrinogen deposition renders fibrinogen volume imaging ideally suited to detect chronic, temporally accumulating BBB abnormalities. Detection of focal fibrin deposits may be superior to assessing transient diffusion of soluble dextrans in whole brain extracts (Bien-Ly et al., 2015), since the latter might lack the sensitivity to detect BBB abnormalities in chronic neurodegenerative diseases (Montagne et al., 2017; Petersen et al., 2018). Given the prominence and critical contribution of cerebrovascular dysfunction to the onset and progression of cognitive decline in AD and vascular dementia (Iadecola, 2013; Montagne et al., 2017), emerging therapies targeting fibrin or other aspects of cerebrovascular dysfunction (Petersen et al., 2018; Ryu et al., 2018; Strickland, 2018; Sweeney et al., 2018) may greatly advance the treatment of cognitive disorders.

STAR METHODS

CONTACT FOR REAGENT AND RESOURCE SHARING

Further information and requests for resources and reagents should be directed to and will be fulfilled by the Lead Contact, Katerina Akassoglou (kakassoglou@gladstone.ucsf.edu).

EXPERIMENTAL MODEL AND SUBJECT DETAILS

Animals—B6.Cg-Tg(Thy1-YFP)HJrs/J (*Thy1-YFP*) (Feng et al., 2000), B6.129P-*Cx3cr1^{tm1Litt}*/J (*Cx3cr1$^{GFP/GFP}$*) (Jung et al., 2000), B6.129S4-*Itgam^{tm1Myd}*/J (*Itgam$^{-/-}$*) (Coxon et al., 1996), and B6.Cg-Tg(APPSwFlLon,PSEN1*M146L*L286V) 6799Vas/Mmjax (5XFAD) (Oakley et al., 2006) mice were obtained from The Jackson Laboratory. *Fga$^{-/-}$* (Suh et al., 1995) and *Fgg$^{\gamma390-396A}$* mice (Flick et al., 2004) were obtained from Dr. Jay Degen (University of Cincinnati, OH, USA). Transgenic mice expressing hAPP with the Swedish and Indiana FAD mutations (line J20) were generated and housed at the Gladstone Institutes (Mucke et al., 2000). Thy1-*YFP*-H mice were crossed with *Cx3cr1$^{GFP/GFP}$* mice to generate *Thy1-YFP:Cx3cr1$^{GFP/+}$* mice, *Itgam$^{-/-}$* and *Thy1-YFP* mice were crossed to generate *Thy1-YFP:Itgam$^{-/-}$* mice, and 5XFAD mice were crossed with *Fgg$^{\gamma390-396A}$* mice to generate 5XFAD:*Fgg$^{\gamma390-396A}$* mice. Mice were housed under a 12:12 light/dark cycle, 55 ± 5% relative humidity, and a temperature of 20 ± 2°C with access to standard laboratory chow and water *ad libitum.* They were housed in social groups of a maximum of 5 mice

each in standard mouse housing cages and bedding. Only mice that had undergone cranial window surgery were housed singly to avoid damage to the cranial window inflicted by cage mates. All single-housed mice were provided with cage enrichment, i.e., a cardboard or hard-plastic house-like hiding place and tissue paper. For husbandry, one male and one female were housed together with a maximum of one litter permitted. Mice were weaned at postnatal day 21. All animal procedures were performed under the guidelines set by the Institutional Animal Care and Use Committee at the University of California, San Francisco (IACUC protocol number AN173418-01).

Human brain tissue—Human brain tissue was collected after informed consent to perform an autopsy was obtained from the next-of-kin, in accordance with the Declaration of Helsinki. All procedures were approved by the UCSF institutional review board. Tissue was provided by the Neurodegenerative Disease Brain Bank at the University of California, San Francisco. Blocks of the lateral temporo-occipital cortex were dissected from five patients with AD and three NDCTRL subjects. Age range was 70–94 years, female/male percentage was 38%, Braak stage and Thal Phase NDCTRLs: II and 0–2, respectively; for AD: IV-VI and 4–5, respectively. The tissue was formalin-fixed for 72 h and was stored in PBS containing 0.05% sodium azide at 4°C.

METHOD DETAILS

Fibrinogen iDISCO in Mouse and Human Brain—Mouse brain tissue was processed as described in the iDISCO immunolabeling protocol (https://idisco.info, December 2016) using either the methanol pretreatment protocol or the alternative method as specified. Mice were perfused with PBS followed by fixation with 4% paraformaldehyde (PFA) in PBS. The brains were post-fixed overnight at 4°C in 4% PFA in PBS and 1 h at room temperature (RT), and were subsequently washed three times in PBS. Primary antibodies used were rat anti-CD31 (1:20; BD Biosciences) and rabbit anti-fibrinogen (1:1000; kind gift from Drs. Jay Degen and Eric Mullins, Department of Pediatrics, Cincinnati Children's Hospital, Cincinnati, OH, USA). Congo Red was added to the secondary antibody incubation buffer at a final concentration of 10 μM. For CD31 and fibrinogen double staining, the alternative pretreatment protocol was used instead of the methanol pretreatment step. Donkey anti-rat Cy3 or Alexa 568 (1:80; Life Technologies) and donkey anti-rabbit Alexa647 (1:500; Life Technologies) were used as secondary antibodies. After clearing, the samples were imaged using a Nikon AZ-100 light sheet microscope equipped with a Vortran 4-line laser launch (50% laser power), an Andor Zyla 5.5 camera, and a 2×/0.2 AZ Plan Apo objective lens to obtain large-volume images. For high-resolution, small-volume images an Olympus Fluoview 1000 confocal microscope equipped with a 20×/0.5 NA objective lens was used. Image processing and analysis were performed with Imaris and ImageJ. Quantification was performed by observers blinded to the mouse age and genotype.

Human temporo-occipital cortex was provided by the Neurodegenerative Disease Brain Bank, University of California at San Francisco. Brain samples were fixed for 72 h in formalin at 4°C following *post mortem* dissection and were stored in PBS/0.05% sodium azide at 4°C thereafter. The fixed tissue was cut into ~1.5-mm thick sections and was processed as described in the official iDISCO immunolabeling protocol following the most

current steps as outlined in the online protocol (https://idisco.info, December 2016) using the methanol pretreatment step and the following modifications of the steps described in the online protocol: 1) Bleaching in 5% hydrogen peroxide in methanol: 36 h; 2) initial two clearing steps in dichloromethane/methanol: 30 min each. Primary antibodies used were sheep anti-human fibrinogen (1:100; US Biological), guinea pig anti-human CD31 (1:100; Synaptic Systems), and rabbit anti-human amyloid β (1:100; IBL-America). Secondary antibodies used were donkey anti-sheep Cy3, donkey antiguinea pig Alexa 488, and donkey anti-rabbit Alexa 647 (1:200; Jackson ImmunoResearch). Brain tissue was incubated in the primary antibody and secondary antibody solution for 72 hours each. Images were acquired using an Olympus Fluoview 1000 confocal microscope equipped with a 20×/0.5 NA objective with acquisition using a 1-photon 543 nm and 633 nm laser to excite the Cy3 and Alexa647 fluorophores and a two-photon Mai Tai eHP DeepSee Ti:sapphire laser (pulse width <70 fs, tuning range 690–1040 nm; Spectra-Physics/Newport) tuned at 940 nm to excite the Alexa488 fluorophore. Image processing was performed in ImageJ.

Immunohistochemistry—Dissection of brains and immunohistochemistry were performed as previously described (Ryu et al., 2015), with modifications. Mice were transcardially perfused with 4% paraformaldehyde (PFA) under ketamine/xylazine anesthesia. The brains were dissected, post-fixed in 4% PFA, and processed for free-floating immunohistochemistry. Sections were blocked with 10% normal donkey serum in PBS with 0.2% Triton X-100, and were incubated with the respective primary antibodies O/N at 4°C antibody diluent (3% normal donkey serum in PBS with 0.1% Triton X-100). Primary antibodies used were mouse anti-amyloid β (6E10; Biolegend; 1:400), goat anti- Iba1 (Novus; 1:500), rat anti-LAMP1 (Developmental Studies Hybridoma Bank, USA; 1:200), guinea pig anti-synaptophysin (Synaptic Systems; 1:1500), and chicken anti-MAP2 (BioLegend; 1:5000). The sections were washed in PBS, followed by a 2-h incubation at RT with Alexa Fluor 488-, 594-, and/or 647-conjugated secondary antibodies (Jackson ImmunoResearch) diluted 1:800, 1:800, and 1:600, respectively, in antibody diluent. Following washing in PBS, the sections were mounted on glass slides and were coverslipped with Prolong Gold antifading agent (Invitrogen). Images were acquired using an Olympus FluoView 1000 confocal microscope equipped with water-immersed objectives (20 × 0.5 NA or 40 × 0.75 NA). Image J (National Institutes of Health,) and MATLAB® (The MathWorks, Inc.) were used for image analysis. Depending on the staining, quantification was performed on thresholded, binary images or counting of cells or morphological structures by researchers blind to the mouse genotype.

Cranial Window Surgery—Mice were kept at 37°C using a heating pad during all surgical and imaging procedures. Surgery was performed under ketamine/xylazine anesthesia (100/10 mg/kg body weight). Following shaving of the head, disinfection of the skin, and local s.c. injection of 2% lidocaine, an incision was made to expose the skull. The skull was thoroughly dried by removing all bone-attached membrane and fat tissue. A circular moat of about 3 mm in diameter was drilled over the somatosensory (S1HL/S1FL) cortex until the thinned bone flexed under gentle pressure of a micro scalpel blade (Nordland Blade #6900, Salvin Dental). A custom-designed (eMachineShop, Mahwah, NJ, USA) steel head bar that included an imaging chamber was positioned over the craniotomy and was

firmly affixed to the skull with cyanoacrylate glue and Metabond® dental cement. A drop of pre-warmed (37°C) artificial cerebrospinal fluid (ACSF, HEPES-based; in mM: 125 NaCl, 10 glucose, 10 HEPES, 3.1 $CaCl_2$, 2.7 KCl, and 1.3 $MgCl_2$; pH 7.4) was applied to the bone island. After ~1 min, the bone island was gently lifted off with a micro scalpel blade (Nordland Blade #6900), followed by gentle flushing of the dura mater with pre-warmed ACSF to clean and remove potentially occurring dural bleedings. A drop of ACSF was placed on top of the dura mater, and the craniotomy was closed and sealed off using a round glass coverslip (3 mm in diameter, type 0; Warner Instruments) which was fixed to the skull and sealed with Flow- It™ ALC™ composite (Pentron) cured under UV light. Lidocaine gel (2%) was applied to the skin around the skull/Metabond®. Imaging experiments were performed 14–17 days after surgery. Mice were excluded if there were signs of (sub-) dural hemorrhage underneath the cranial window and/or morphological changes in the leptomeninengeal vessels (such as swelling, tortuosity, or leakage) as these events would cause inflammatory and other neurodegenerative responses unrelated to the experimental design.

In Vivo Two-Photon Brain Microscopy—An Ultima IV two-photon microscope (Prairie Technologies/Bruker) equipped with a Mai Tai eHP DeepSee and an Insight X3 Ti:sapphire femtosecond laser (pulse width <120 fs, tuning range 690–1040 nm (Mai Tai) and 680–1300 nm (Insight X3), repetition rate 80 MHz; Spectra-Physics/Newport) were used, tuned to an excitation wavelength of 840–1100 nm depending on the fluorophore(s) used. Imaging was performed ~100μm below the dura mater in the somatosensory cortex for vascular, dendrite, spine, microglia, and amyloid imaging. A Nikon 40×0.8 NA, a Nikon 10×0.4 NA, or an Olympus 25×1.05 NA water-immersion lens was used. Images were acquired in galvo scan mode at 512×512 pixels, 1.5 Hz, and a 0.2μm z-step. The maximum laser power exiting the objective was <40 mW during all imaging experiments. An IR-blocking filter and 520-nm dichroic were placed in the primary emission beam path before the detectors. A 573-nm dichroic and a 607/45-nm and 542/27-nm bandpass filter were used to separate Alexa-594/Texas Red/rhodamine and YFP emission, respectively; a 458-nm dichroic and a 494/41-nm and 433/24-nm bandpass filter were used to separate GFP and Methoxy-X04 emission, respectively.

In Vivo Brain Imaging and Cortical Microinjections—In vivo imaging in the cortex was performed as described (Davalos et al., 2012), with modifications. Mice were randomly assigned to the experimental groups. The glass coverslip that had been placed over the craniotomy on the surgery day (see "Cranial window surgery" above) was carefully removed. A 100-μl solution of 70-kDa rhodamine-conjugated dextran or 10-kDa Cascade Blue dextran (Thermo Fisher Scientific) in ACSF was injected retro-orbitally to label the vasculature, after which the mouse was fixed under the 2P microscope. For the baseline dendrite, spine, and microglia morphology and density imaging experiments, glass electrodes (tip diameter: 1 μm, shaft length: 4 mm) were pulled and were filled with ACSF, 1.5 mg/mL fibrinogen diluted in ACSF, plasma from WT mice, or plasma from $Fga^{-/-}$ mice. All solutions were mixed with 3% 70-kDa Texas Red-conjugated dextran (Thermo Scientific) to enable visualization of the injection liquid. The diluted fibrinogen, WT plasma, and $Fga^{-/-}$ plasma samples and glass electrodes were kept at 37°C until filling of the

electrodes. The filled electrodes were subsequently inserted at a depth of ~100–150 μm below the dura mater using a micromanipulator (Narishige), coordinated by visualization through the microscope under epifluorescence light. An *xyz* stack of $100 \times 100 \times 60$ μm was set around the electrode tip, and a small volume (~5–10 pL) of the respective solution was injected with a pressure injector (Narishige) at a pressure of 0.35–0.6 bar during simultaneous imaging of the neurites, spines, and microglia at $4 \times$ optical zoom ($40 \times$ objective lens). Additional *xyz* stacks were acquired with the $40 \times$ objective lens at $1 \times$ and $2 \times$ optical zoom and with the $10 \times$ objective lens at $1 \times$ optical zoom to create overview maps of the vasculature and dendritic structures for relocation of the same imaging site. A new coverslip was placed and sealed over the craniotomy. Three days later, the same imaging area was relocated using the $10 \times$ and $40 \times$ vascular overview maps and was re-imaged as described above.

In Vivo Brain Imaging of Fibrinogen Deposits and Dendritic Spine Turnover in AD Mice—Dendritic spine turnover was quantified as described previously (Bittner et al., 2012), with modifications. 5XFAD and hAPP-J20 mice were stereotactically injected with AAV1.hSyn.eGFP.WPRE.bGH in the somatosensory cortex to fluorescently label dendrites and spines. Following the injection, a craniotomy was prepared as described above ("Cranial window surgery"). Alexa 594-labeled fibrinogen (1.5 mg/mL; ThermoFisher Scientific) was administered i.v. at day 12 and day 13 following surgery; Methoxy-X04 (5 mg/kg; Tocris Biosciences) was administered i.p. on day 13 following surgery to label Aβ plaques. Dendritic spines with and without Alexa 594-labeled fibrinogen deposits and which were located <50 and >50 μm of an Aβ plaque were imaged using 2P microscopy at 840 nm and 920 nm and a $40 \times$ objective at $4 \times$ optical zoom as described under "In vivo brain imaging and cortical microinjections". The same location was imaged 14 days later.

In Vivo Apocynin Treatment—A cranial window as described above was made in *Thy1-YFP* mice. Mice were randomly assigned to the experimental groups. Apocynin (3 mM in ACSF; Calbiochem) was applied to the exposed dura mater and was injected intraperitoneally (5 mg/kg BW diluted in saline) 45 min before image acquisition. The dura mater was bathed with the apocynin solution also during image acquisition. A mixture of 1.5 mg/mL fibrinogen, 3 mM apocynin, and 3% 70-kDa Texas Red-conjugated dextran diluted in ACSF was injected in the area to be imaged as described above. Image acquisition at baseline and at day 3 was performed as described under "In vivo brain imaging and cortical microinjections".

In Vivo ROS Imaging—In vivo imaging of ROS was performed as described previously (McLellan et al., 2003), with modifications. The glass coverslip that had been placed over the craniotomy on the surgery day (see "Cranial window surgery" above) was carefully removed, and a 200-μM solution of Amplex Ultra Red (ThermoFisher Scientific) in ACSF was applied to the exposed dura mater for 30 min shielded from light. Following several washes with ACSF, fibrinogen or ACSF was injected into the cortex. Images were acquired at 840 nm (detection of red-fluorescent resorufin) and 920 nm (detection of microglia [GFP] and neurites [YFP]) within the injection site. The cranial window was sealed with a glass coverslip (see "Cranial window surgery" above), and was removed at day 3 after the ACSF

or fibrinogen injection and baseline Amplex Ultra Red image acquisition. The dura mater was gently but thoroughly washed, a 200-μM solution of Amplex Ultra Red was applied to the exposed dura mater and washed off as described above, and images were acquired within the ACSF or fibrinogen injection site at 840 nm and 920 nm.

Behavioral Experiments—All behavioral experiments were performed at the Gladstone Behavioral Core by researchers blind to genotype before and during the behavioral tasks, and during data analyses and imaging quantification. Mice were randomly assigned to the behavioral assays. Only male mice were used to avoid the potential confounding effect of the female hormonal cycle on behavior. The Hot Plate Test consisted of a black anodized, aluminum plate. The apparatus was cleaned with Vimoba before and after use, and with 70% alcohol between the testing of each mouse. Mice were transferred to the testing room 60 min prior to testing to acclimate. The surface of the hot plate was heated to a constant temperature of 52°C as measured by a built-in digital thermometer.During testing, the mice were placed in a clear, open-ended cylindrical enclosure, which was placed on top of the hot plate. The latency to respond with either a hindpaw lick, hindpaw flick, or jump (which ever was observed first) was measured and the experimenter stopped the timer when the response was observed. The mouse was immediately removed from the hot plate and returned to its home cage. Each animal was only tested once. To prevent injury, the maximum latency was 30 sec.

Active Place Avoidance Training was used to measure amygdala/hippocampal-dependent visual-spatial learning and memory. Mice with better visual-spatial learning and memory should exhibit longer paths, fewer entries into the shock zone, fewer shocks, longer latencies to enter the zone, and higher maximal avoidance measures over the course of the 3 days of training and relative to the Habituation baseline. The Probe test was used to measure the reference memory of the animals for the aversive zone without the reminder of the unconditioned stimulus (shock) being present. Mice with better visual-spatial learning and memory should exhibit fewer entries into the shock zone and longer latencies to the 1st entrance with fewer shocks. Mice with poor reference and/or working memory exhibit more entries into the shock zone, shorter latencies to enter the aversive zone repeatedly, and higher number of shocks. The Reinstatement test was used to counteract any extinction effects of the Probe test and measured the dependence of effective avoidance behavior on the presence of the unconditioned stimulus or shock. Mice with poor reference memory but intact working memory entered the zone quickly but showed longer latencies to the 2nd entrance and decreased number of entrances and shocks relative to the Probe test.

Testing was performed using the Place Avoidance system and Tracker software from BioSignal Corp. Distinct black & white visual cues were placed on the walls of the room surrounding the apparatus. The mice were placed inside a Plexiglas cylinder of 40-cm diameter covered with a lid that was resting on a metal grid connected to the electric shock modulator. The cylinder and grid were cleaned with 70% alcohol between trials. Each trial lasted 10 min and each animal underwent one trial per day. The Probe/Reinstatement test on Day 5 was split into two 5-min segments, with the Probe segment first with the current source (shock) turned off while the Reinstatement segment occurred during the second 5-min phase with the current source being turned back on but not until the mouse completely

had completely left the shock zone if it was still present after the first 5 min. The grid arena could be rotated at 1 RPM (either CW or CCW) during the trials such that the animal had to actively navigate against the rotation of the arena to avoid entering the aversive zone (circle, box, or wedge of space designated by the experimenter as the aversive zone) which was fixed relative to the external configuration of spatial cues surrounding the arena. The path of each mouse within the arena was tracked with the Tracker software video. When the animal entered the aversive zone, the Tracker activated a 0.2-mA current source for 500 ms, which was repeated every 1.5 sec until the mouse had left the zone.

Day 1:Habituation. A stationary 60° wedge of the arena was designated as the aversive zone, which was either a fixed location on the rotating arena or relative to the extra-maze cues. This established a baseline of path activity within the arena prior to the start of avoidance training. Mice underwent one 10-min trial in which the current source (shock) was not activated to allow the mice to habituate to the apparatus while it was rotating. The dependent measures included total path length, number of entrances, latency to 1st entrance, path to 1st entrance, number of shocks, speed, maximum time of avoidance, maximum path of avoidance, latency to 2nd entrance, and path to 2nd entrance. Days 2–4: Avoidance Training. The mice underwent one 10-min trial per day with the current source (shock) activated. Any time a mouse was tracked as entering the aversive zone a 0.2-mA shock was delivered for 500 ms and repeatedly every 1.5 s thereafter until the mouse had left the zone. Day 5: Probe/ Reinstatement Testing. The 10-min trial was split into two 5-min phases. The first phase was the Probe Test in which the current source was turned off in order to assess memory performance for the aversive zone without the presence of the unconditioned stimulus. After 5 min had elapsed, the current source was turned on only when the mouse had clearly left the aversive zone. This Reinstatement Test continued for another 5 min.

The behavior in an open field was measured in an automated clear plastic chamber ($41 \times 41 \times 30$ cm) with two 16×16 photo-beam arrays detecting horizontal and vertical movements (Flex-Field/Open Field Photobeam Activity System [San Diego Instruments]). The apparatus was cleaned with 70% alcohol between testing of each mouse. Total test time was 15 min. Mice were transferred to the testing room 60 min prior to testing to acclimate to the testing conditions. During testing, the mice were placed in one of the four identical clear plastic chambers for 15 min. Activity levels, exploratory behaviors, and anxiety-like responses to a new environment were assessed using measurements of movement and grooming in an open space. Total movements in the outer periphery and center of the open field were recorded. Ambulatory and fine movements were also recorded. Fine movements were defined as movements breaking <3 photobeams; ambulatory movements were defined as movements breaking >3 photobeams. Ambulatory movements were interpreted as walking behavior.

QUANTIFICATION AND STATISTICAL ANALYSIS

Quantification of in Vivo Imaging Data—Dendrite and spine imaging: The $100 \times 100 \times 60$ μm xyz stacks acquired around the glass electrode tip at baseline (day 0/day of micro-injection) and at the same location on day 3 were processed using ImageJ. The number of dendrites at day 3 (injection model) was calculated as percentage of that at baseline/day 0.

To calculate changes or equality in spine numbers at day 3 compared to those at baseline, dendrites were identified that were present in both the baseline and the day 3 imaging stacks. The number of spines on these dendrites at day 3 was calculated as percentage of that at baseline. Quantification was performed by researchers blinded to the injection agent (fibrinogen or ACSF). Spines in the 5XFAD and hAPP-J20 mice were quantified as follows. The images acquired on day 0 (baseline) and day 14 were separated into the respective z-series channels [spines/dendrites (green), fibrinogen (red), and Aβ (blue)]. Quantification of the green channel (spines) was performed blinded to the other two channels (fibrinogen and/or Aβ). Subsequently, spine turnover on day 14 as compared to day 0 was quantified in the z-stacks on dendrites present in both the day-0 and day-14 images. The dendrite/spine z-stacks were then merged with the fibrinogen z-stacks. The presence or absence of fibrinogen deposits and distance of fibrinogen deposits from the quantified spines were measured. Subsequently, the Aβ z-stacks were merged with the combined fibrinogen- dendrite/spine z-stacks stacks. The presence or absence of Aβ deposits and distance of the Aβ deposits to the quantified spines and co-localization with fibrinogen were measured. Using this blinding method, spines were identified that were on 1) dendrites with Alexa 594-labeled fibrinogen deposits and located >50 pm of an Aβ plaque; 2) dendrites located <50 pm of an Aβ plaque without fibrinogen deposits; 3) dendrites located <50 pm of an Aβ plaque with fibrinogen deposits; and 4) dendrites located >50 pm of an Aβ plaque and fibrinogen deposits. The number of spines in each of these four distinct areas at day 14 was calculated as percentage of that atbaseline/day 0 imaging. Images acquired in *Thy1-YFP:Cx3cr1*[GFP/+] mice were spectrally unmixed to separate YFP from GFP signals.

ROS imaging: The extent of Amplex Red fluorescence within the micro-injection site at day 3 following local fibrinogen or ACSF micro-injection was calculated as the percentage of the extent of the Amplex Red fluorescence at day 0/baseline. Quantification was performed by researchers blinded to the injection agent (fibrinogen or ACSF).

Statistical Analyses—Data are expressed as the mean ± standard error of the mean. Differences between experimental conditions were analyzed with GraphPad Prism software (version 7; GraphPad, Inc.) or MATLAB® (version 2017; The MathWorks, Inc.). Data distribution was assumed to be normal although this was not formally tested. The significance of the differences between spine density at day 0 and day 14 was determined using a two-tailed paired Student's *t*-test. The significance of the differences in the number of dendrites and spines or ROS signal between baseline/day 0 and day 3 in each mouse and between each genotype or between each treatment protocol was determined either using a two-tailed unpaired Student's *t*-test or one-way analysis of variance (ANOVA) and Bonferroni *post hoc* analysis as specified in the respective figure legends. Oneway ANOVA with Bonferroni *post hoc* analysis was used for the statistical analysis of the histological data. The behavioral data were analyzed using two-way ANOVA with multiple comparisons and Bonferroni or Holm-Sidak *post hoc* analysis as specified in the legend of Figure 4. In all analyses, $p < 0.05$ was considered statistically significant.

Supplementary Material

Refer to Web version on PubMed Central for supplementary material.

ACKNOWLEDGEMENTS

REFERENCES

Adams RA, Bauer J, Flick MJ, Sikorski SL, Nuriel T, Lassmann H, Degen JL, and Akassoglou K (2007). The fibrin-derived gamma377-395 peptide inhibits microglia activation and suppresses relapsing paralysis in central nervous system autoimmune disease. J Exp Med 204, 571–582. [PubMed: 17339406]

Akoudad S, Wolters FJ, Viswanathan A, de Bruijn RF, van der Lugt A, Hofman A, Koudstaal PJ., Ikram MA, and Vernooij MW (2016). Association of cerebral microbleeds with cognitive decline and dementia. JAMA Neurol 73, 934–943. [PubMed: 27271785]

Barker R, Ashby EL, Wellington D, Barrow VM., Palmer JC, Kehoe PG, Esiri MM, and Love S (2014). Pathophysiology of white matter perfusion in Alzheimer's disease and vascular dementia. Brain 137, 1524–1532. [PubMed: 24618270]

Bien-Ly N, Boswell CA, Jeet S, Beach TG, Hoyte K, Luk W, Shihadeh V, Ulufatu S, Foreman O, Lu Y, et al. (2015). Lack of widespread BBB disruption in Alzheimer's disease models: Focus on therapeutic antibodies. Neuron 88, 289–297. [PubMed: 26494278]

Bittner T, Burgold S, Dorostkar MM, Fuhrmann M, Wegenast-Braun BM, Schmidt B, Kretzschmar H, and Herms J (2012). Amyloid plaque formation precedes dendritic spine loss. Acta Neuropathol 124, 797–807. [PubMed: 22993126]

Boros BD, Greathouse KM, Gentry EG, Curtis KA, Birchall EL, Gearing M, and Herskowitz JH (2017). Dendritic spines provide cognitive resilience against Alzheimer's disease. Ann Neurol 82, 602–614. [PubMed: 28921611]

Butovsky O, and Weiner HL (2018). Microglial signatures and their role in health and disease. Nat Rev Neurosci. 19, 622–635. [PubMed: 30206328]

Cortes-Canteli M, Paul J, Norris EH, Bronstein R, Ahn HJ, Zamolodchikov D, Bhuvanendran S, Fenz KM, and Strickland S (2010). Fibrinogen and beta-amyloid association alters thrombosis and fibrinolysis: a possible contributing factor to Alzheimer's disease. Neuron 66, 695–709. [PubMed: 20547128]

Coxon A, Rieu P, Barkalow FJ, Askari S, Sharpe AH, von Andrian UH, Arnaout MA, and Mayadas TN (1996). A novel role for the beta 2 integrin CD11b/CD18 in neutrophil apoptosis: a homeostatic mechanism in inflammation. Immunity 5, 653–666. [PubMed: 8986723]

Czirr E, Castello NA, Mosher KI, Castellano JM, Hinkson IV, Lucin KM, Baeza-Raja B, Ryu JK, Li L, Farina SN, et al. (2017). Microglial complement receptor 3 regulates brain Abeta levels through secreted proteolytic activity. J Exp Med 214, 1081–1092. [PubMed: 28298456]

Davalos D, Kyu Ryu J, Merlini M, Baeten KM, Le Moan N, Petersen MA, Deerinck TJ, Smirnoff DS, Bedard C, Hakozaki H, et al. (2012). Fibrinogen-induced perivascular microglial clustering is required for the development of axonal damage in neuroinflammation.Nat Commun 3, 1227. [PubMed: 23187627]

De Strooper B, and Karran E (2016). The Cellular Phase of Alzheimer's Disease. Cell 164, 603–615. [PubMed: 26871627]

Feng G, Mellor RH, Bernstein M, Keller-Peck C, Nguyen QT, Wallace M, Nerbonne JM, Lichtman JW, and Sanes JR (2000). Imaging neuronal subsets in transgenic mice expressing multiple spectral variants of GFP. Neuron 28, 41–51. [PubMed: 11086982]

Flick MJ, Du X, Witte DP, Jirouskova M, Soloviev DA, Busuttil SJ, Plow EF, and Degen JL (2004). Leukocyte engagement of fibrin(ogen) via the integrin receptor alphaMbeta2/Mac-1 is critical for host inflammatory response in vivo. J Clin Invest 113, 1596–1606. [PubMed: 15173886]

Gowrishankar S, Yuan P, Wu Y, Schrag M, Paradise S, Grutzendler J, De Camilli P, and Ferguson SM (2015). Massive accumulation of luminal protease-deficient axonal lysosomes at Alzheimer's disease amyloid plaques. Proc Natl Acad Sci U S A 112, E3699–3708. [PubMed: 26124111]

Hartz AM, Bauer B, Soldner EL, Wolf A, Boy S, Backhaus R, Mihaljevic I, Bogdahn U, Klunemann HH, Schuierer G, et al. (2012). Amyloid-beta contributes to blood-brain barrier leakage in transgenic human amyloid precursor protein mice and in humans with cerebral amyloid angiopathy. Stroke 43, 514–523. [PubMed: 22116809]

Haslund-Vinding J, McBean G, Jaquet V, and Vilhardt F (2017). NADPH oxidases in oxidant production by microglia: activating receptors, pharmacology and association with disease. Br J Pharmacol 174, 1733–1749. [PubMed: 26750203]

Hong S, Beja-Glasser VF, Nfonoyim BM, Frouin A, Li S, Ramakrishnan S, Merry KM, Shi Q, Rosenthal A, Barres BA, et al. (2016). Complement and microglia mediate early synapse loss in Alzheimer mouse models. Science 352, 712–716. [PubMed: 27033548]

Iadecola C (2013). The pathobiology of vascular dementia. Neuron 80, 844–866. [PubMed: 24267647]

Jung S, Aliberti J, Graemmel P, Sunshine MJ, Kreutzberg GW, Sher A, and Littman DR (2000). Analysis of fractalkine receptor CX(3)CR1 function by targeted deletion and green fluorescent protein reporter gene insertion. Mol Cell Biol 20, 4106–4114. [PubMed: 10805752]

Kirkwood CM, Ciuchta J, Ikonomovic MD, Fish KN, Abrahamson EE, Murray PS., Klunk WE, and Sweet RA (2013). Dendritic spine density, morphology, and fibrillar actin content surrounding amyloid-beta plaques in a mouse model of amyloid-beta deposition. J Neuropathol Exp Neurol 72, 791–800. [PubMed: 23860033]

Lassmann H (2011). Mechanisms of neurodegeneration shared between multiple sclerosis and Alzheimer's disease. J Neural Transm 118, 747–752. [PubMed: 21373761]

McLellan ME, Kajdasz ST, Hyman BT, and Bacskai BJ (2003). In vivo imaging of reactive oxygen species specifically associated with thioflavine S-positive amyloid plaques by multiphoton microscopy. J Neurosci 23, 2212–2217. [PubMed: 12657680]

Merlini M, Wanner D, and Nitsch RM (2016). Tau pathology-dependent remodelling of cerebral arteries precedes Alzheimer's disease-related microvascular cerebral amyloid angiopathy. Acta Neuropathol 131, 737–752. [PubMed: 26988843]

Montagne A, Nikolakopoulou AM, Zhao Z, Sagare AP, Si G, Lazic D, Barnes SR, Daianu M, Ramanathan A, Go A, et al. (2018). Pericyte degeneration causes white matter dysfunction in the mouse central nervous system. Nat Med 24, 326–337. [PubMed: 29400711]

Montagne A, Zhao Z, and Zlokovic BV (2017). Alzheimer's disease: A matter of blood-brain barrier dysfunction? J Exp Med 214, 3151–3169. [PubMed: 29061693]

Mucke L, Masliah E, Yu GQ, Mallory M, Rockenstein EM, Tatsuno G, Hu K, Kholodenko D, Johnson-Wood K, and McConlogue L (2000). High-level neuronal expression of abeta 1-42 in wild-type human amyloid protein precursor transgenic mice: synaptotoxicity without plaque formation. J Neurosci 20, 4050–4058. [PubMed: 10818140]

Oakley H, Cole SL, Logan S, Maus E, Shao P, Craft J, Guillozet-Bongaarts A, Ohno M, Disterhoft J, Van Eldik L, et al. (2006). Intraneuronal beta-amyloid aggregates, neurodegeneration, and neuron loss in transgenic mice with five familial Alzheimer's disease mutations: potential factors in amyloid plaque formation. J Neurosci 26, 10129–10140. [PubMed: 17021169]

Pastalkova E, Serrano P, Pinkhasova D, Wallace E, Fenton AA, and Sacktor TC (2006). Storage of spatial information by the maintenance mechanism of LTP. Science 313, 1141–1144. [PubMed: 16931766]

Petersen MA, Ryu JK, and Akassoglou K (2018). Fibrinogen in neurological diseases: mechanisms, imaging and therapeutics. Nat Rev Neurosci 19, 283–301. [PubMed: 29618808]

Petersen MA, Ryu JK, Chang KJ, Etxeberria A, Bardehle S, Mendiola AS, Kamau- Devers W, Fancy SPJ, Thor A, Bushong EA, et al. (2017). Fibrinogen activates BMP signaling in oligodendrocyte progenitor cells and inhibits remyelination after vascular damage. Neuron 96, 1003–1012 e1007. [PubMed: 29103804]

Rabin JS, Schultz AP, Hedden T, Viswanathan A, Marshall GA, Kilpatrick E, Klein H, Buckley RF, Yang HS, Properzi M, et al. (2018). Interactive associations of vascular risk and beta-amyloid burden with cognitive decline in clinically normal elderly individuals: Findings from the Harvard aging brain study. JAMA Neurol. 75, 1124–1131. [PubMed: 29799986]

Renier N, Wu Z, Simon DJ, Yang J, Ariel P, and Tessier-Lavigne M (2014). iDISCO: a simple, rapid method to immunolabel large tissue samples for volume imaging. Cell 159, 896–910. [PubMed: 25417164]

Ryu JK, Petersen MA, Murray SG, Baeten KM, Meyer-Franke A, Chan JP, Vagena E, Bedard C, Machado MR, Coronado PE., et al. (2015). Blood coagulation protein fibrinogen promotes autoimmunity and demyelination via chemokine release and antigen presentation. Nat Commun 6, 8164. [PubMed: 26353940]

Ryu JK, Rafalski VA., Meyer-Franke A, Adams RA, Poda SB, Rios Coronado PE, Pedersen LO, Menon V, Baeten KM, Sikorski SL, et al. (2018). Fibrin-targeting immunotherapy protects against neuroinflammation and neurodegeneration. Nat Immunol 19, 1212–1223. [PubMed: 30323343]

Shinkai Y, Yoshimura M, Ito Y, Odaka A, Suzuki N, Yanagisawa K, and Ihara Y (1995). Amyloid beta-proteins 1-40 and 1-42(43) in the soluble fraction of extra- and intracranial blood vessels. Ann Neurol 38, 421–428. [PubMed: 7668828]

Strickland S (2018). Blood will out: vascular contributions to Alzheimer's disease. J Clin Invest 128, 556–563. [PubMed: 29388925]

Suh TT, Holmback K, Jensen NJ, Daugherty CC, Small K, Simon DI, Potter S, and Degen JL (1995). Resolution of spontaneous bleeding events but failure of pregnancy in fibrinogen-deficient mice. Genes Dev 9, 2020–2033. [PubMed: 7649481]

Sweeney MD, Sagare AP, and Zlokovic BV (2018). Blood-brain barrier breakdown in Alzheimer disease and other neurodegenerative disorders. Nat Rev Neurol. 14, 133–150. [PubMed: 29377008]

Tsai J, Grutzendler J, Duff K, and Gan WB (2004). Fibrillar amyloid deposition leads to local synaptic abnormalities and breakage of neuronal branches. Nat Neurosci 7, 1181–1183. [PubMed: 15475950]

Vemuri P, Lesnick TG, Przybelski SA, Knopman DS, Preboske GM, Kantarci K, Raman MR, Machulda MM, Mielke MM, Lowe VJ., et al. (2015). Vascular and amyloid pathologies are independent predictors of cognitive decline in normal elderly. Brain 138, 761–771. [PubMed: 25595145]

Weinhard L, di Bartolomei G, Bolasco G, Machado P, Schieber NL, Neniskyte U, Exiga M, Vadisiute A, Raggioli A, Schertel A, et al. (2018). Microglia remodel synapses by presynaptic trogocytosis and spine head filopodia induction. Nat Commun 9, 1228. [PubMed: 29581545]

Zamolodchikov D, Berk-Rauch HE, Oren DA, Stor DS, Singh PK., Kawasaki M, Aso K, Strickland S, and Ahn HJ (2016). Biochemical and structural analysis of the interaction between beta-amyloid and fibrinogen. Blood 128, 1144–1151. [PubMed: 27389717]

HIGHLIGHTS

- Fibrinogen is a blood-derived inducer of spine elimination

- Fibrinogen induces Aβ-independent synapse loss in AD mice

- 3D volume imaging of BBB disruption and Aβ in cleared human AD brain

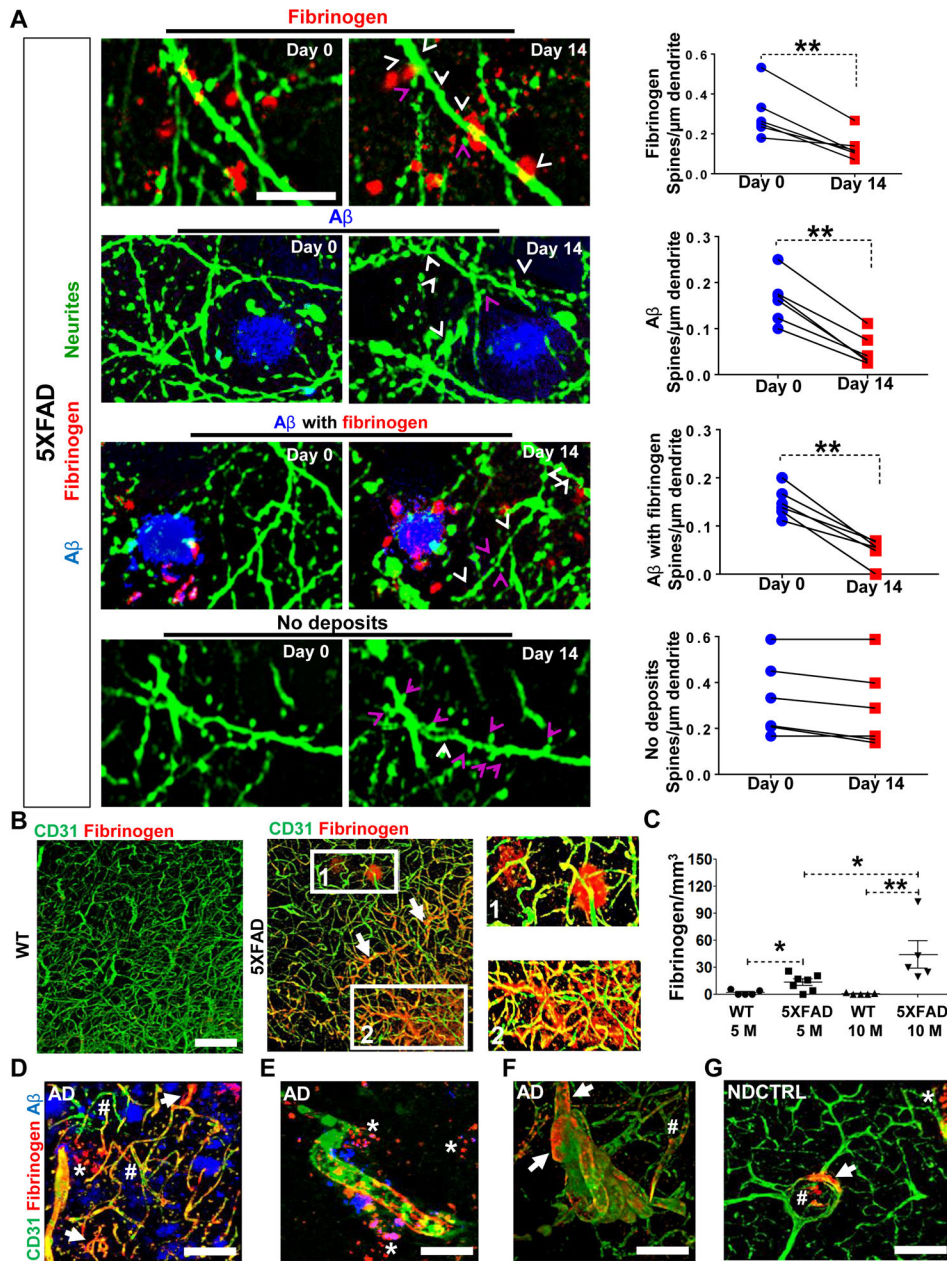- Genetic inhibition of fibrinogen–CD11b binding improves cognition in AD mice

Figure 1. Dendritic Spine Elimination around Fibrinogen Deposits in 5XFAD Mice

(A) Longitudinal in vivo 2P imaging of turnover of spines (AAV-synapsin:GFP, green), fibrinogen (Alexa594-labeled fibrinogen, red), and Aβ plaques (Methoxy-X04, blue) in the cortex of 7-08-month-old 5XFAD mice. Images were acquired in the same cortical area on Day 0 and Day 14. "*Fibrinogen*": Spines in areas with fibrinogen deposits located >50 μm from Aβ plaques. "*Aβ*": Spines located within 50 μm from Aβ plaques without fibrinogen deposits. "*Aβ with fibrinogen*": Spines located within 50 μm from Aβ plaques with fibrinogen deposits. "*No deposits*": Spines located >50 μm from either Aβ plaques or fibrinogen deposits. Arrowheads indicate stable (magenta) and lost (white) spines on day 14 as compared to day 0. Maximum z-projections are shown. Scale bar = 10 μm. Dendritic

spine density was assessed on 30–36 dendrites for each mouse. Values are mean ± SEM. n = 6 mice. **p < 0.001 by two-tailed unpaired Student's *t*-tests.

(B) 3D immunolabeling of cleared brain of a 10-month-old 5XFAD mouse and WT littermate control for CD31 (green) and fibrinogen (red). Fibrinogen deposits (*inset* 1) and perivascular fibrinogen (arrows and *inset* 2) are shown in the 5XFAD hippocampus, but not in WT control mice. Scale bar = 100 μm. Quantification of hippocampal fibrinogen deposits in WT and 5XFAD mice at 5 and 10 months (M) of age. n = 5–7 mice per group. Values are mean ± SEM. *p < 0.05, **p < 0.01 by two-way ANOVA with Bonferroni *post hoc* test..

(C–F) 3D immunolabeling of cleared brains from patients with AD and NDCTRL subjects stained for CD31 (green), fibrinogen (red), and Aβ (blue). Arrows and asterisks indicate vessel-associated and parenchymal fibrinogen, respectively; # indicates intravascular fibrinogen. Magenta in (D) indicates Aβ-associated fibrinogen. (E) Vascular tortuosity observed in three out of the five AD brains. Representative images are shown. Scale bars = 75 μm (C), 25 μm (D), 25 μm (E), and 75 μm (F).
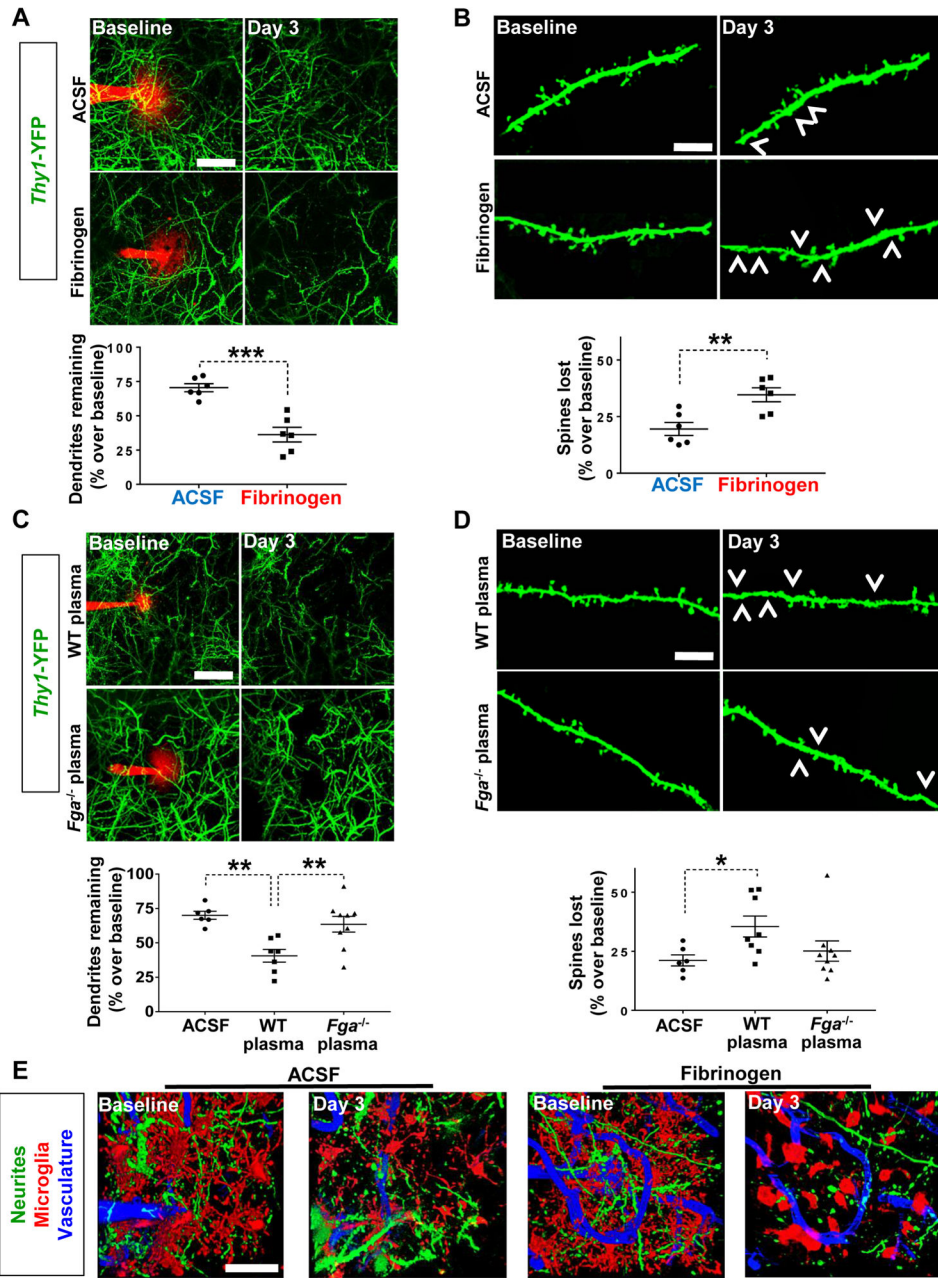
Figure 2. Fibrinogen is Sufficient to Induce Dendrite and Spine Loss in the Healthy Brain

(A) Longitudinal in vivo 2P imaging of dendrites (green) in the cortex of *Thy1-YFP* mice before (Baseline) and after local injection of vehicle (ACSF) or human fibrinogen (red) (Day 3). The injection electrode is indicated in red. Maximum z-projections are shown. Scale bar = 25 μm. All dendrites remaining over baseline were quantified per mouse. n = 6 mice per condition. Values are mean ± SEM. **p < 0.01, ***p < 0.001 by two-tailed unpaired Student's *t*-test.

(B) Longitudinal in vivo 2P imaging of spine turnover in the cortex of the *Thy1-YFP* mice shown in (A). Arrowheads indicate lost spines on day 3. Maximum z-projections are shown. Scale bar = 10 μm. Quantification of spines lost over baseline. 40–70 spines were followed

per mouse. n = 6 mice per condition. Values are mean ± SEM. **p < 0.01, ***p < 0.001 by two-tailed unpaired Student's *t*-test.

(C) Longitudinal in vivo 2P imaging of dendrites (green) in the cortex of *Thy1-YFP* mice before (Baseline) and after local injection of plasma from WT or *Fga*$^{−/−}$ mice (Day 3). Injection electrode is indicated in red. Maximum z-projections are shown. Scale bar = 25 μm. All dendrites remaining over baseline were quantified per mouse. ACSF: n = 6, WT plasma: n = 8, *Fga*$^{−/−}$ plasma: n = 9 mice. Values are mean ± SEM. **p < 0.01 by one-way ANOVA and Bonferroni *post hoc* analysis.

(D) Longitudinal in vivo 2P imaging of spine turnover in the cortex of the *Thy1-YFP* mice shown in (C). Injection electrode is indicated in red. Maximum z-projections are shown. Scale bar = 10 μm. Quantification of spines lost over baseline. 40–70 spines were followed per mouse. ACSF: n = 6 mice, WT plasma: n = 8 mice, *Fga*$^{−/−}$ plasma: n = 9 mice. Values are mean ± SEM. *p < 0.05 by one-way ANOVA and Bonferroni *post hoc* analysis.

(E) Longitudinal in vivo 2P imaging of microglia (GFP, pseudo-colored in red), dendrites (YFP, yellow-green), and blood vessels (Cascade Blue 10kDa dextran, blue) in the cortex of a 12-week-old *Thy1-YFP: Cx3cr1*$^{GFP/+}$ mouse before (Baseline) and after local injection of ACSF vehicle or fibrinogen (Day 3). Representative 3D volume z-projections are shown. Scale bar = 25 μm.
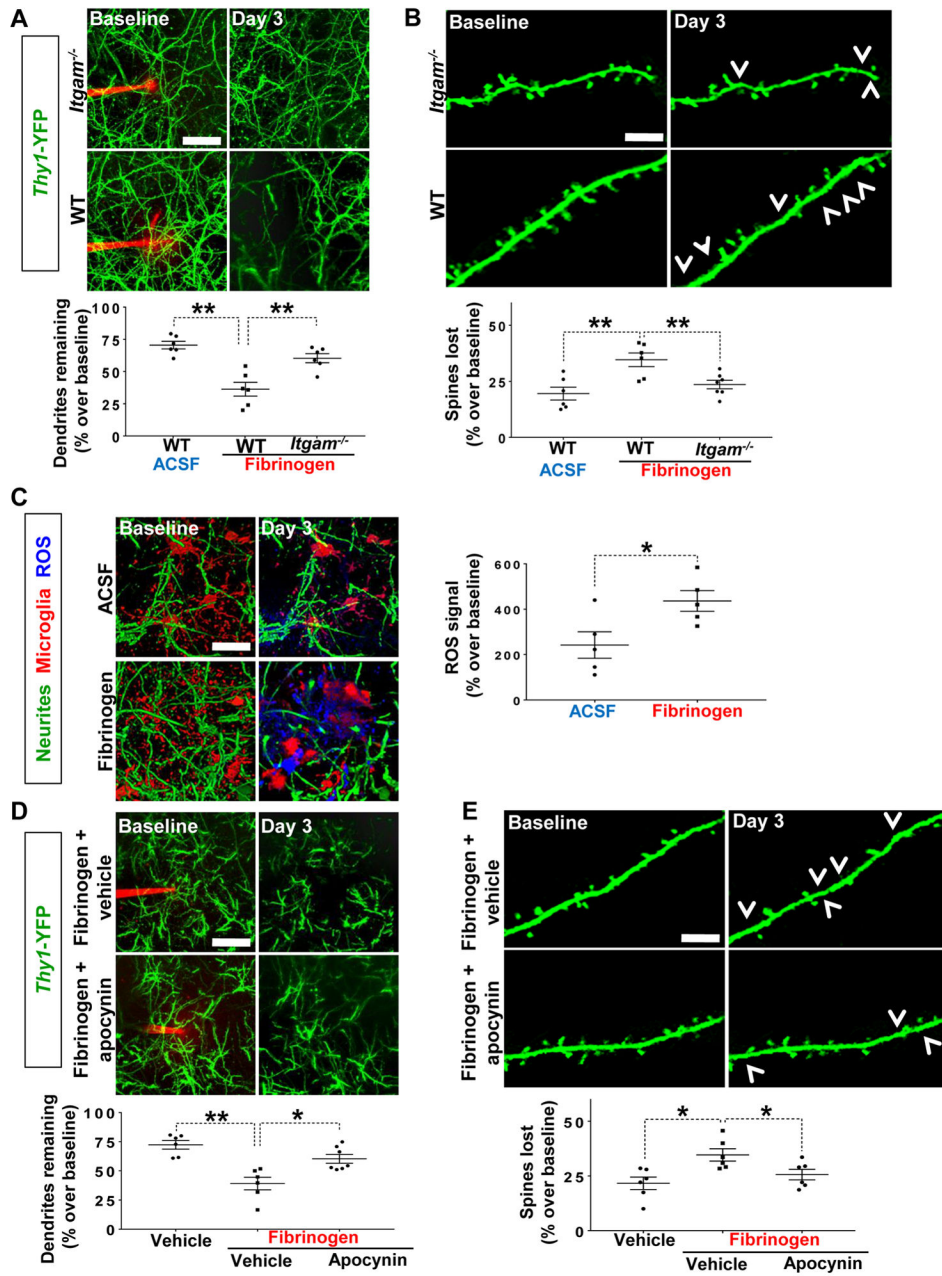
Figure 3. Fibrinogen induces Dendrite and Spine Loss through CD11b/CD18 Receptor and ROS Generation

(A) Longitudinal in vivo 2P imaging of dendrites (green) in the cortex of control *Thy1-YFP* mice and *Thy1-YFP:Itgam*^{−/−} mice before (Baseline) and on day 3 after local injection of vehicle (ACSF) or fibrinogen. Injection electrode is indicated in red. Maximum z-projections are shown. Scale bar = 25 μm. All dendrites remaining over baseline were quantified per mouse. n = 6–7 mice per group. Values are mean ± SEM. **p < 0.01 by one-way ANOVA with Bonferroni *post hoc* analysis.

(B) Longitudinal in vivo 2P imaging of spine turnover in the cortex of the *Thy1-YFP* and Thy1-*YFP:ItgamT*^{−/−} mice shown in (A). Arrowheads indicate lost spines on day 3,

compared to baseline. Maximum z-projections are shown. Scale bar = 10 μm. Quantification of spines lost over baseline. 40–70 spines were followed per mouse. n = 6–7 mice per group. Values are mean ± SEM. **p < 0.01 by one-way ANOVA with Bonferroni *post hoc* analysis.

(C) Longitudinal in vivo 2P imaging of microglia (GFP, pseudo-colored in red), dendrites (yellow-green), and ROS (Amplex® Ultra Red, pseudo-colored in blue) in the cortex of a 10-week-old *Thy1-YFP:Cx3cr1GFP/+* mouse before (Baseline) and after local injection of vehicle (ACSF) or fibrinogen (Day 3). 3D volume z projections are shown. Scale bar = 25 μm. Quantification of ROS signal. n = 5 mice per condition. Values are mean ± SEM. *p < 0.05 by two-tailed unpaired Student's *t*-test.

(D) Longitudinal in vivo 2P imaging of dendrites (green) in the cortex of *Thy1-YFP* mice before (Baseline) and after local injection of fibrinogen + vehicle (ACSF) or fibrinogen + apocynin (Day 3). Injection electrode is indicated in red. Maximum z-projections are shown. Scale bar = 25 μm. All dendrites remaining over baseline were quantified per mouse. Values are mean ± SEM. *p < 0.05, **p < 0.01 by one-way ANOVA and Bonferroni *post hoc* analysis.

(E) Spine turnover in the cortex of the *Thy1-YFP* mice shown in (D). Arrowheads indicate lost spines at day 3. Injection electrode is indicated in red. Maximum z-projections are shown. Scale bar = 10 μm. Quantification of spines lost over baseline.

40–70 spines were followed per mouse. n = 6–7 mice per group. Values are mean ± SEM. *p < 0.05 by one-way ANOVA and Bonferroni *post hoc* analysis.
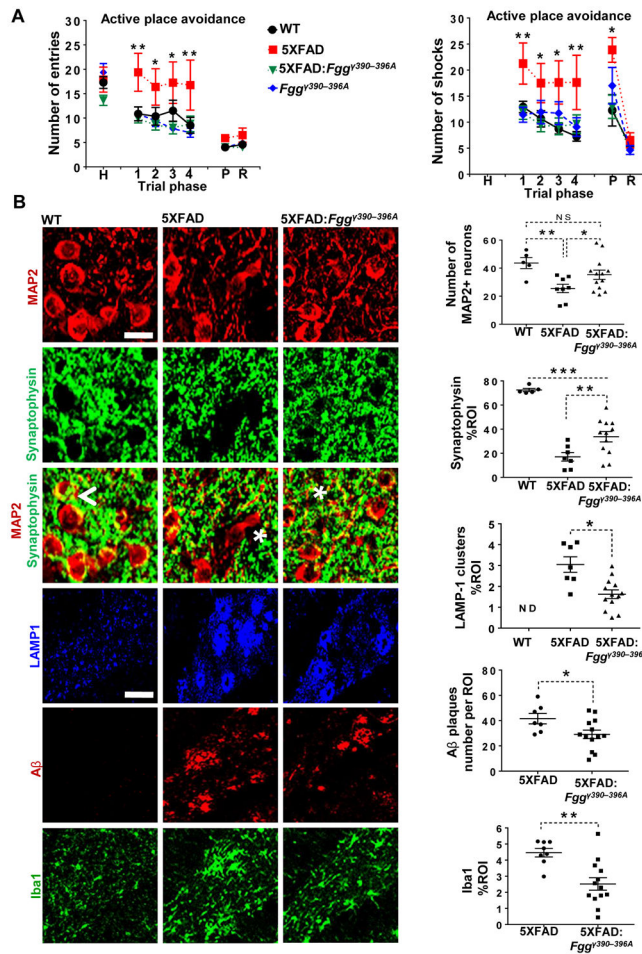
Figure 4. Mutation of the Fibrinogen Binding Site to CD11b Prevents Neurodegeneration and Cognitive Impairment

(A) Spatial learning and memory in 9–10-month-old mice of the indicated genotype with the active place avoidance test. Habituation to the apparatus (H) was followed by training trials 1–4, a probe trial (P), and a reinstatement trial (R). Number of entries into the aversive zone (left) and number of shocks received after entry into this zone (right) were used as the main outcome measures. WT: n = 14, 5XFAD: n = 8, 5XFAD:$Fgg^{\gamma390-396A}$: n = 16, $Fgg^{\gamma390-396A}$: n = 11 mice. Values are mean ± SEM. *p < 0.05 **, p < 0.01 by two-way ANOVA with Bonferroni's *post hoc* test.

(B) Maximum z-projections showing neuronal somata and dendrites (MAP2), presynaptic terminals (synaptophysin), lysosomes (LAMP-1), amyloid β Aβ; 6E10 antibody), and microglia (Iba1) in the dentate gyrus of the WT, 5XFAD, and 5XFAD:$Fgg^{\gamma390-396A}$ mice tested behaviorally in (A). Arrow head in the merged MAP2–synaptophysin image of the WT mouse indicates close association of synaptophysin staining with MAP2-positive neuronal somata. Asterisks in the merged MAP2–synaptophysin images indicate loss of this association. Scale bar = 25 μm. Three brain sections were analyzed per mouse for staining quantification. ROI, region of interest. ND, not detected (large clusters of LAMP-1-positive structures). WT: n = 5, 5XFAD: n = 8, 5XFAD:$Fgg^{\gamma390-396A}$: n = 13 mice. Values are mean

± SEM. *p < 0.05, **p < 0.01, ***p < 0.001 by one-way ANOVA and Bonferroni *post hoc* test or two-tailed unpaired Student's *t*-test.